This copy of the ESI replaces the previous version published on 29 June 2022

Supporting Information

The ligand field in low-crystallinity metal–organic frameworks investigated by soft X-ray core-level absorption spectroscopy

Kohei Yamagami,[a] Haruka Yoshino,[b,c,d] Hirona Yamagishi,[e] Hiroyuki Setoyama[f], Arata Tanaka,[g] Ryo Ohtani,[b] Masaaki Ohba,[b] and Hiroki Wadati[a,h]

[a] Institute for Solid State Physics (ISSP), The University of Tokyo, Kashiwanoha, Chiba 277-8581, Japan.
Present address: Japan Synchrotron Radiation Research Institute (JASRI), 1-1-1, Sayo-cho, Sayo-gun, Hyogo 679–5198, Japan
E-mail: kohei.yamagami@spring8.or.jp
[b] Department of Chemistry, Graduate School of Science, Kyushu University, Motooka 744, Nishi-ku, Fukuoka 819-0395, Japan
[c] Institute for Materials Research, Tohoku University, 2-1-1 Katahira, Aoba-ku, Sendai 980-8577, Japan
[d] Department of Chemistry, Graduate School of Science, Tohoku University, 6-3 Aramaki-Aza-Aoba, Aoba-ku, Sendai 980-8578, Japan
[e] Synchrotron Radiation Center, Ritsumeikan University, Kusatsu, Shiga 525-0058, Japan
f Kyushu Synchrotron Light Research Center, 8-7 Yayoigaoka, Tosu 841-0005, Saga, Japan
[g] Department of Quantum Matter, ADSM, Hiroshima University, Higashihiroshima, Hiroshima 739-8530, Japan
[h] Graduate School of Material Science, University of Hyogo, 3-2-1 Kouto, Kamigori-cho, Ako-gun, Hyogo 678-1297, Japan

Materials

All chemicals were used without further purification. $M(H_2O)_2[T(CN)_4]\cdot 4H_2O$ (***MT*-H_2O**; *M* = Mn, Fe, Co, Ni; *T* = Ni, Pd) and dehydrated phases of $M([T(CN)_4]$ (***MT***) were synthesized according to a previously reported method [1-3].

$Mn(H_2O)_2[Ni(CN)_4]\cdot 4H_2O$ (**MnNi-H_2O**)

A solution of $K_2[Ni(CN)_4]\cdot H_2O$ (198.7 mg, 0.767 mmol) in H_2O (100 mL) was added to a solution of $MnCl_2\cdot 4H_2O$ (151.8 mg, 0.767 mmol) in H_2O (80 mL) at room temperature. White powder samples were obtained after stirring for 24 h. Yield: 64.5%.

$Fe(H_2O)_2[Ni(CN)_4]\cdot 4H_2O$ (**FeNi-H_2O**)

FeNi-H_2O was prepared as white powder samples in a similar method to that used for **MnNi-H_2O**, except for the use of $Fe(NH_4)_2(SO_4)_2\cdot 6H_2O$ (300.4 mg, 0.766 mmol) in degassed H_2O (80 mL). Yield: 70.1%.

$Co(H_2O)_2[Ni(CN)_4]\cdot 4H_2O$ (**CoNi-H_2O**)

CoNi-H_2O was prepared as pink powder samples in a similar method to that used for **MnNi-H_2O**, except for the use of $CoCl_2\cdot 6H_2O$ (180.4 mg, 0.758 mmol). Yield: 74.5%.

$Ni(H_2O)_2[Ni(CN)_4]\cdot 4H_2O$ (**NiNi-H_2O**)

NiNi-H_2O was prepared as a light-blue powder using a method similar to that used for **MnNi-H_2O**, except for the use of $NiCl_2\cdot 6H_2O$ (180.4 mg, 0.759 mmol). Yield: 72.6%.

$Ni(H_2O)_2[Pd(CN)_4]\cdot 4H_2O$ (**NiPd-H_2O**)

NiPd-H_2O was prepared as light-blue powder samples in a similar method to that used for **NiNi-H_2O**, except for the use of $K_2[Pd(CN)_4]\cdot H_2O$ (260.1 mg, 0.759 mmol). Yield: 77.8%.

$M[Ni(CN)_4]$ (***M*Ni**) and $Ni[Pd(CN)_4]$ (**NiPd**)

This copy of the ESI replaces the previous version published on 29 June 2022

The dehydrated powder samples of ***M*Ni** and **NiPd** were obtained by heating ***M*Ni-H_2O** and **NiPd-H_2O** under vacuum at 400 K for 6 h.

Ni *K*-edge XAS spectra and EXAFS analysis

Ni *K*-edge measurements of ***M*Ni** (*M* = Mn, Fe, Co, Ni) and **NiPd** were performed at BL-11 of the SAGA Light Source. A Si (111) double crystal monochromator was installed for measurements in the range of $h\nu$ = 2.1−23 keV with a photon energy resolution ($h\nu/\Delta h\nu$) of 10^4 to 10^3. Ni *K*-edge XAS spectra were obtained in transmission mode at room temperature using two ionization chambers, as shown in **Fig. S6(a)**. The absorbance [$-\log(I_1/I_0)$] was calculated from the incident X-ray intensity (I_0) and the transmitted X-ray intensity (I_1). A mixture of He 50%/N_2 50% and Ar 15%/N_2 85% was used as the ionization gas for I_0 and I_1, respectively. The photon energy was calibrated using NiO. The samples were diluted with high-purity boron nitride to the appropriate concentration for XAS measurements and molded into pellets in an Ar-filled glovebox. The pellet samples were subsequently sealed in a polyethylene case. The analyzed Ni *K*-edge XAS data were processed using Athena and Artemis software [6].

Fig. S6(b) shows the Ni *K*-edge XAS spectra of ***M*Ni** and **NiPd**. The main peak at 8347.5 eV is assigned to the 1*s* → 4*p* absorption, while the pre-edge around 8336 eV corresponds to the 1*s* → 3*d* electric quadrupole transition. The same spectral features, including in the pre-edge (labeled as P_1 and P_3) among **MnNi**, **FeNi**, and **CoNi**, were observed, indicating the same electronic states and local structures at the C-coordinating Ni^{2+} ions. This is consistent with the transition metal (***M***)-independent Ni $L_{2,3}$-edge XAS spectra of **MnNi**, **FeNi**, and **CoNi**, (**Fig. S7**). On the other hand, in **NiPd**, the pre-edge has a different peak position (labeled as P_2) from ***M*Ni** since the Ni ions of **NiPd** are coordinated only with nitrogen ligands. The averaged spectra of **CoNi** and **NiPd** at a 1:1 ratio can reproduce the Ni *K*-edge XAS spectra of **NiNi** (**Fig. S6(c)**), confirming that the XAS spectra of **NiNi** is composed of both N- and C-coordinating Ni ions. As presented in the main text, we carried out a similar analysis to the Ni $L_{2,3}$-edge XAS spectra in **Fig. 2** and arrived at the same conclusion.

Furthermore, we observed Ni *K*-edge extended x-ray absorption fine structure (EXAFS) oscillation (**Fig.6(d)**). The radial distance spectra of Ni in ***M*Ni** (*M* = Ni, Co, Fe, Mn) and **NiPd** obtained by the Fourier transform (**Fig.6(e)**) show three peaks at ~1.4 Å (A), ~2.5 Å (B), and ~4.5 Å (C). **Fig.S6(f)** illustrates the correspondence between observed peaks A-C and each atomic distance in ***M*Ni**

and **NiPd**. In **CoNi**, **FeNi**, and **MnNi**, peaks A, B, and C are assigned as the Ni-C, Ni-N, and Ni-*M* (*M* = Co, Fe, Mn), respectively. The *M*-independent Ni-C and Ni-N distances relates to the triple covalent bonds, while the *M*-dependent Ni-M distance relates to the coordinating bond, being consistent with previous *K*-edge EXAFS analysis [3]. In **NiPd**, because of nitrogen coordinating Ni, peaks A, B, and C are assigned as the Ni-N, Ni-C, and Ni-Pd, respectively. Ni-Pd distance is longer than that any other *M*-Ni (*M* = Mn, Fe, Co, Ni) distance, corresponding to the IR spectra (**Fig.S2 (a) and (b)**). It found that Ni-N distance in **NiPd** is shorter than *M*-N one in ***M*Ni** (*M* = Co, Fe, Mn) [3], implying the stronger orbital hybridization between Ni 3*d* and N 2*p* orbitals. On the other hand, in **NiNi**, because of the coexistence of both nitrogen and carbon coordinating Ni, peaks A and B contain of both Ni-C and Ni-N distances. The similar Ni-N distance in **NiNi** to that in **NiPd** would give that the local 3*d* electronic state of nitrogen coordinating Ni is similar between **NiNi** and **NiPd**.

Configuration-interaction single cluster model calculations

We carried out MLFT calculations within the configuration-interaction $[M\mathrm{N}_4]^{10-}$ single cluster under S_p and T_d symmetry (**Fig. S8(a)**). This cluster is composed of one M^{2+} cation and four N^{3-} anions, whose electronic states originate from the ionic picture and charge transfer as a perturbation. The initial ground state of the cluster $|\Psi_{\mathrm{GS}}\rangle$ can be described as a linear combination of the nominal $2p^6 3d^n$ M ion states $|d^n\rangle$ and the $2p^6 3d^{n+m}\underline{L}^m$ charge transfer states due to covalency $|d^{n+m}\underline{L}^m\rangle$ below:

$$|\Psi_{\mathrm{GS}}\rangle = c_0|d^n\rangle + c_1|d^{n+1}\underline{L}\rangle + c_2|d^{n+2}\underline{L}^2\rangle \ldots + c_m|d^{n+m}\underline{L}^m\rangle$$

where $\underline{L}$ and $c_m^2 = \langle d^{n+m}\underline{L}^m|d^{n+m}\underline{L}^m\rangle$ give the ligand hole and the weight of each configuration, respectively. In the same procedure, the XAS final state $|\Psi_{\mathrm{XAS}}\rangle$ is described by a linear combination of $|p^5 d^{n+1}\rangle$ and $|p^5 d^{n+m}\underline{L}^{m-1}\rangle$ configurations as follows:

$$|\Psi_{\mathrm{XAS}}\rangle = C_0|p^5 d^{n+1}\rangle + C_1|p^5 d^{n+2}\underline{L}\rangle + C_2|p^5 d^{n+3}\underline{L}^2\rangle \ldots + C_m|p^5 d^{n+m}\underline{L}^{m-1}\rangle$$

All the calculations were performed at 300 K using XTLS 9.0 [7]. The intra-atomic parameters of M^{2+} ions, such as the 3*d*-3*d* and 2*p*-3*d* Coulomb and exchange interactions (so-called Slater integrals F^k and G^k), and the 2*p* and 3*d* spin-orbit couplings (ζ) have been obtained by Cowan's code based on the Hartree-Fock method [8]. F^k and G^k values were reduced to 80% for all calculations, whereas the ζ value was reduced to 98% for Co. For T_d symmetry, the core-level spectra were reproduced by tuning parameters, such as the on-site M 3*d* electron Coulomb interaction (U_{dd}), M 2*p* core hole-3*d* electron Coulomb interactions (U_{cd}), crystalline field (CEF) splitting of M 3*d* orbitals (10*Dq*), ligand-to-metal charge-transfer energy (Δ), and covalency-hopping integrals (V_σ and V_π). The sign of 10*Dq* is defined as positive (negative) when the symmetry is O_h (T_d) [9]. The ligand-to-metal charge-transfer energy is the difference in the energy between the M 3*d* and ligand 2*p* states [$E(d^{n+1}\underline{L})$–$E(d^n)$]. $V_\sigma = \frac{2\sqrt{6}}{3}(pd\sigma)$ and V_π =

$\sqrt{\frac{4}{3}(pd\sigma)^2+\frac{8}{9}(pd\pi)^2}$ for T_d symmetry are expressed in terms of Slater-Koster parameters: ($pd\sigma$) and ($pd\pi$) [10], and the schematic of the overlap of the defining wave functions is shown in **Fig. S8(b)**. When V_σ and V_π are zero, the relative energy diagram among each configuration for the initial and XAS final states can be described, as shown in **Fig. S8(c)**. To reproduce the experimental spectra, the Gaussian broadening width was set to approximately 250 meV, whereas the Lorentzian broadening width of *the* L_3- (L_2-) edge was set to 350 meV (≈600 meV). Following previous studies [11,12], the U_{cd} and ($pd\pi$) values were calculated from the ratios U_{cd} = U_{dd}/0.8 and ($pd\pi$) = −($pd\sigma$)/2.2, which allowed us to reduce the parameter space and compare these parameters among ***M*Ni** (*M* = Mn, Fe, Co). Therefore, we optimized three parameters, namely 10*Dq*, ∆, ($pd\sigma$), and U_{dd}, to reproduce the XAS spectra. The ligand bandwidth was approximated as zero in all calculations.

First, we tuned the 10*Dq* value using the simplified point-charged ionic model under T_d symmetry, which is a good starting point to reproduce XAS spectra reflecting localized *M* 3*d* character. **Fig. S9** shows the calculated *M* $L_{2,3}$-edge XAS spectra as functions of 10*Dq*. The simulation results were consistent with previous calculation results. We find that the best 10*Dq* value is in the range of -0.1 eV < 10*Dq* < -1.0 eV since the spectral structure above 10*Dq* = -1.0 eV is completely inconsistent with the experimental XAS results. The optimized 10*Dq* is -0.1±0.05 eV for Mn, -0.35±0.05 eV for Fe, and -0.7±0.1 eV for Co to reproduce the experimental energy difference among each spectral feature (see the line with symbol in Fig. S9).

Hereafter, we will use the optimized 10*Dq* values in the calculations. Second, we tuned the values of Δ and ($pd\sigma$) to elucidate the charge transfer contribution, which is related to chemical covalency. **Fig. S10** shows the calculated XAS spectra as a function of ($pd\sigma$) by changing the Δ value. In Δ = 0.0 eV, the spectra became more asymmetric with increasing ($pd\sigma$). For Mn, this tendency is reasonable because our Mn $L_{2,3}$-edge XAS spectra show that the energy difference among the peak structures is larger than that calculated under the ionic picture (**Fig. S9** and **Fig. 3** in the main text). However, an overly large ($pd\sigma$) value is inconsistent with the Mn L_2-edge spectral shape. In contrast to Mn, we judged

that the finite Δ values could reproduce the XAS results for Fe and Co. To enclose the calculated spectral intensity and the peak positions to the XAS results, the optimized the values of Δ and (*pdσ*) are 0.0 eV, 0.15 eV for Mn, 4.0 eV, 1.0±0.25 eV for Fe and 4.5±1.5 eV, 0.125±0.125 eV for Co, respectively.

Hereafter, we will use the optimized 10*Dq*, Δ, and (*pdσ*) values in calculations. Finally, the U_{dd} values were considered. **Fig. S11** shows the calculated XAS spectra as a function of U_{dd}. We found a negligibly small contribution of U_{dd} to the XAS spectra. In this study, to compare the parameters among 10*Dq*, Δ, and (*pdσ*) in ***M*Ni**, U_{dd} is a constant value of 6.5 eV, which is within the normal range of inorganic compounds [11,12].

In the main text, the best parameters of 10*Dq*, Δ, (*pdσ*), and U_{dd} for Mn, Fe, and Co are summarized in Table 1 and their corresponding calculated spectra are shown in Fig. 3.

The obtained physical parameters can provide information on not only the electronic configuration but also spin state (see table 1 in the main text), we evaluated the validity of the physical parameters using the effectively magnetic moment for paramagnet **MnNi**, **FeNi**, and **CoNi** (*M* = Mn, Fe, Co). In the paramagnetic state, the moment μ_J (in units of Bohr magneton μ_B) is calculated from the equation below

$$\mu_J = g_J\sqrt{J(J+1)} \quad \cdots \quad (1)$$

Where g_J denotes Lange's factor defined as

$$g_J = \frac{3}{2} + \frac{S(S+1) - L(L+1)}{2J(J+1)} \quad \cdots \quad (2)$$

$S(S+1)$, $L(L+1)$, and $J(J+1)$ denotes the eigenvalue for spin angular momentum ($\hat{S}^2$), orbital angular momentum ($\hat{L}^2$), and total angular momentum ($\hat{J}^2, J = L + S$) operators. The experimental value of the effective magnetic moment μ_{eff} can be obtained from the magnetic susceptibility ($\chi_M T$ [in units of emu·K/mol]) and below equation

$$\mu_{\text{eff}} = \sqrt{\frac{3k_B\chi_m T}{N\mu_B^2}} \approx 2.828\sqrt{\chi_M T} \quad \cdots \quad (3)$$

In the main text, the comparison with μ_J values obtained from ionic picture and MLFT calculation results and μ_{eff} value is shown. What is important is the μ_J value for MLFT calculation is closer to μ_{eff} one than that for ionic case, indicating the presence of the LMCT states. Especially in **MnNi**, since the μ_J value can be determined by the spin only due to the d^5 based high spin states (S = 5/2, L = 0), which the large LMCT effect would be important. In fact, the μ_J value obtained for best parameters (Δ, 10Dq, ($pd\sigma$)) = (0, -0.1, 0.15) is closer value (5.9064) to than that (5.9114) for the (Δ, 10Dq, ($pd\sigma$)) = (4, -0.1, 0) case, therefore we judge that the small Δ value in **MnNi** is plausible.

We also performed the MLFT calculations for the Ni^{2+} ions under S_p symmetry. The tuning parameter is the same as those of the T_d symmetry case, while the representation of the CEF splitting and the covalent hopping integral is different. For simplicity, the CEF splitting of the 3d orbitals with respect to the S_p symmetry was varied with the parameter δ as a variable (**Fig. S12(a)**) [9], where δ value corresponds to the CEF splitting between b_{1g} and b_{2g} orbitals. Covalency-hopping integrals were acted on each orbital with ($pd\sigma$) as variable, respectively. Note that these simplified depictions should be used only for qualitative discussions tracking tendencies in spin states and XAS spectral shapes.

At beginning, as the same procedure as the T_d symmetry case, we investigated the δ-dependence of the XAS spectra using the simplified point-charged ionic model. In **Fig.S12(b)**, we found that the boundary between high spin and low spin state was found to exist around δ = 1.7 eV. Based on the experimental fact that the zero total spin number of **NiNi** and **NiPd** and the conventional 10Dq value used for nickel inorganic compounds [14], the δ value was set to 2.0 eV. In the point-charged ionic model, it clearly sees that calculated spectra does not reproduce the experimental spectra because of the absent of the LMCT satellite peak (labeled as Y in the main text).

Next, we investigated the Δ and ($pd\sigma$) dependence of the LMCT satellite peak in Ni $L_{2,3}$-edge XAS spectra. In this calculation, it set U_{dd} = 6.5 eV. It found at **Fig.S12(c)** that the LMCT satellite peak position has strongly ($pd\sigma$) dependence and the ($pd\sigma$) value should be around 2.0 eV in order to reproduce the LMCT satellite peak position. The estimated ($pd\sigma$) value is enough larger than that of

***M*Ni** for T_d symmetry, therefore, we conclude from the MLFT calculation for S_p symmetry that N-coordinating Ni ions of **NiPd** and **NiNi** have the strong orbital hybridization.

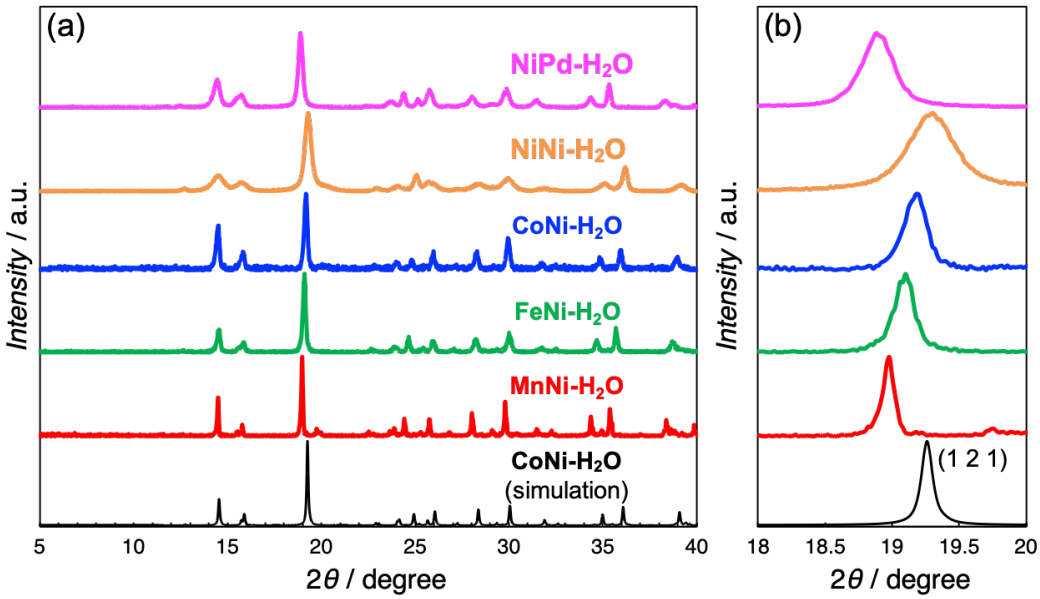

Fig. S1. PXRD patterns of ***M*Ni-H$_2$O** (*M* = Mn, Fe, Co, Ni) and **NiPd-H$_2$O** in the range of (a) 5 – 40° and (b) 18 – 20°.

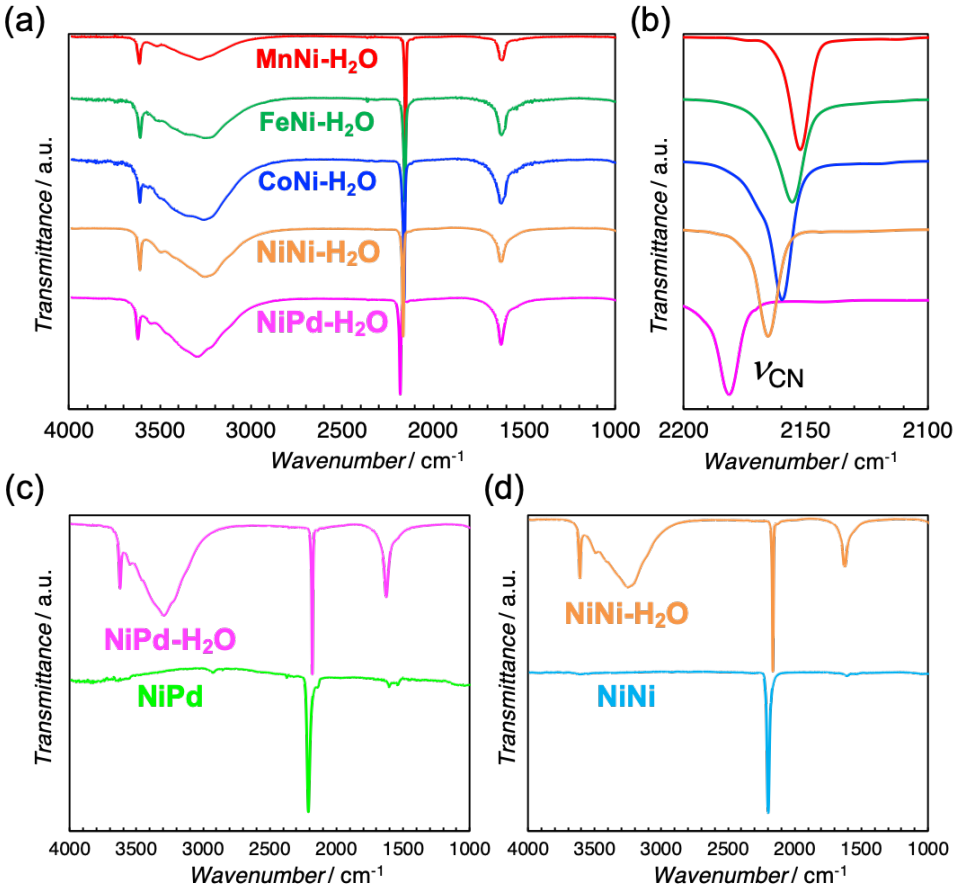

Fig. S2. IR spectra of ***M*Ni-H$_2$O** (M = Mn, Fe, Co, Ni) and **NiPd-H$_2$O** in the range of (a) 4000-1000 cm^{-1} and (b) 2200-2100 cm^{-1},(ν_{CN}). IR spectra of (c) **NiPd-H$_2$O**, **NiPd** and (d) **NiNi-H$_2$O**, **NiNi**.

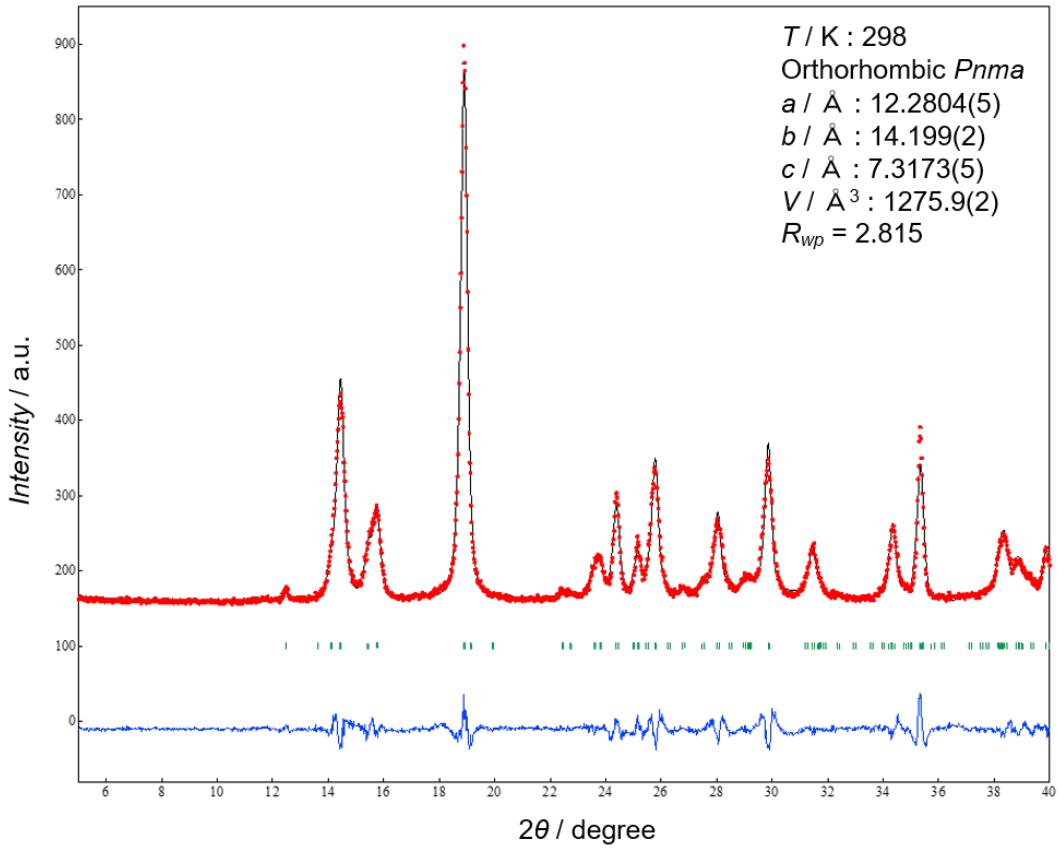

Fig. S3. Le Bail analysis of **NiPd-H_2O** at 298 K with the results of PXRD pattern (λ = 1.5418 Å). Red dots, black line, and blue line represent the observed plots, calculated pattern, and their difference, respectively. Green bars are the calculated positions of the Bragg reflections. The analysis was performed using FOX and RIETAN-FP software.[4,5]

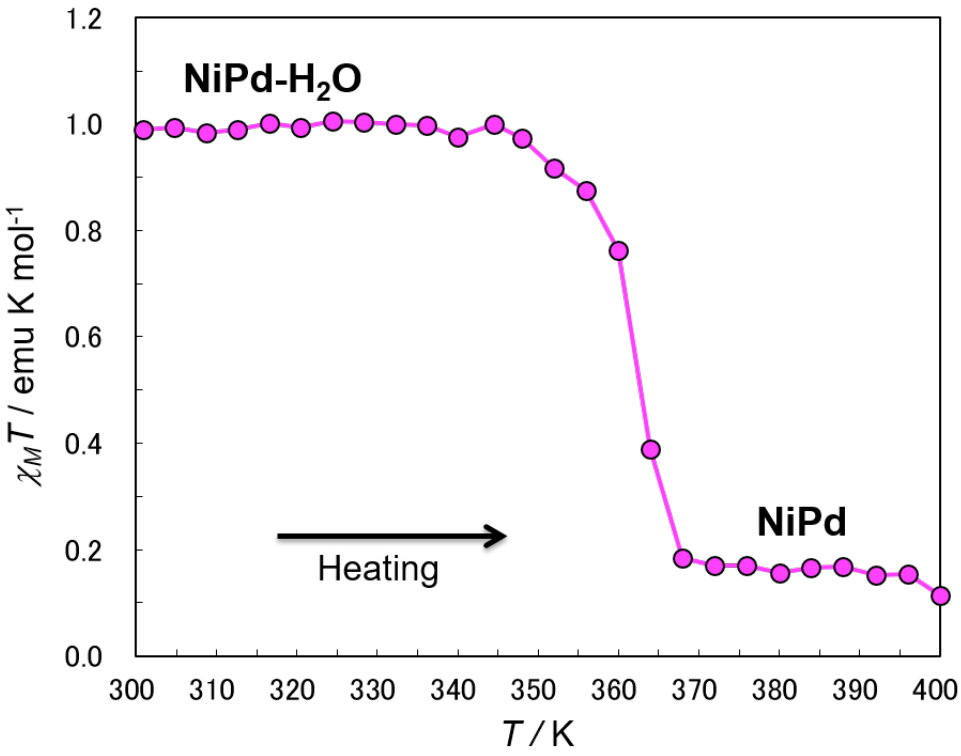

Fig. S4. $\chi_M T$ vs. T plots for **NiPd-H_2O** in the heating process under an applied DC magnetic field of 1000 Oe.

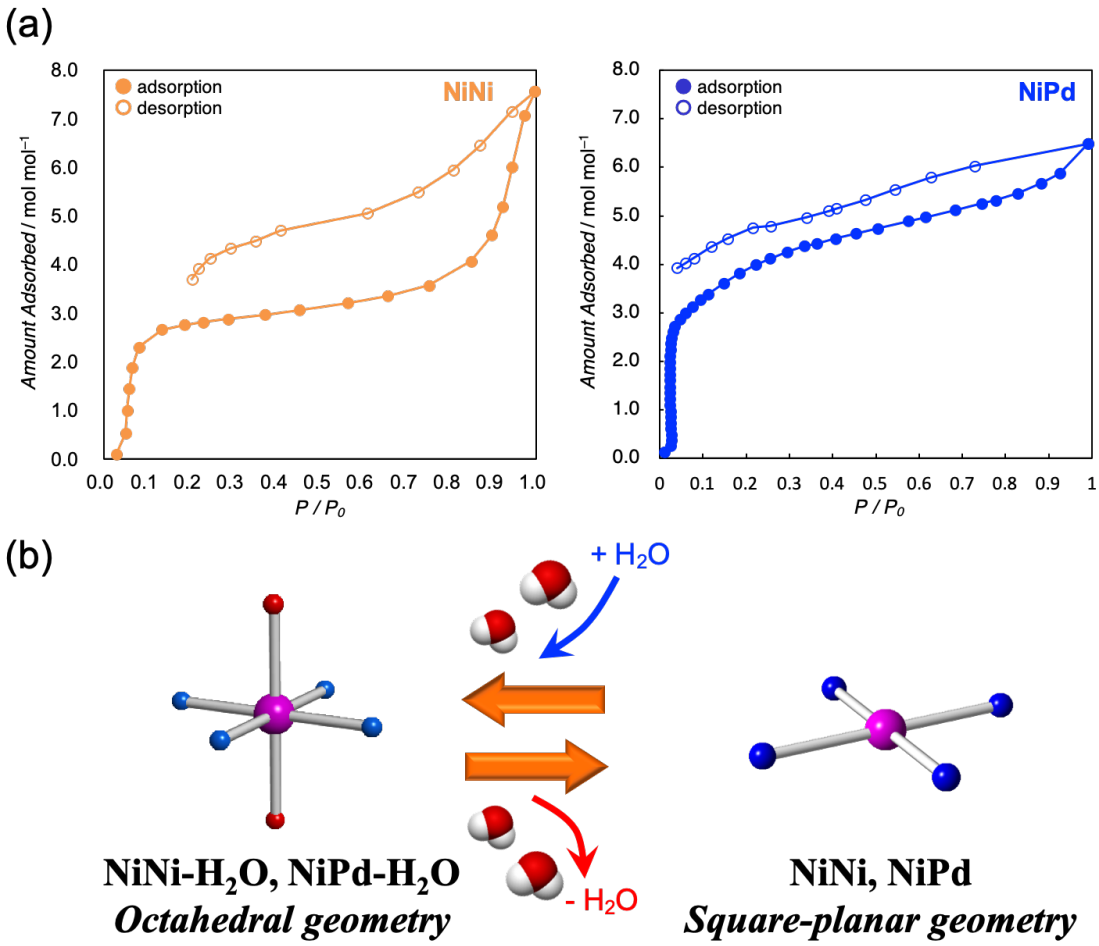

Fig. S5. (a) H_2O adsorption/desorption isotherms of **NiNi** and **NiPd** at 298 K. The filled and open circles display the adsorption and desorption processes, respectively. The solid lines represent a guide for easier viewing. (b) Schematic illustration of the change in the coordination geometry for **NiNi** and **NiPd** along with H_2O ads/desorption process.

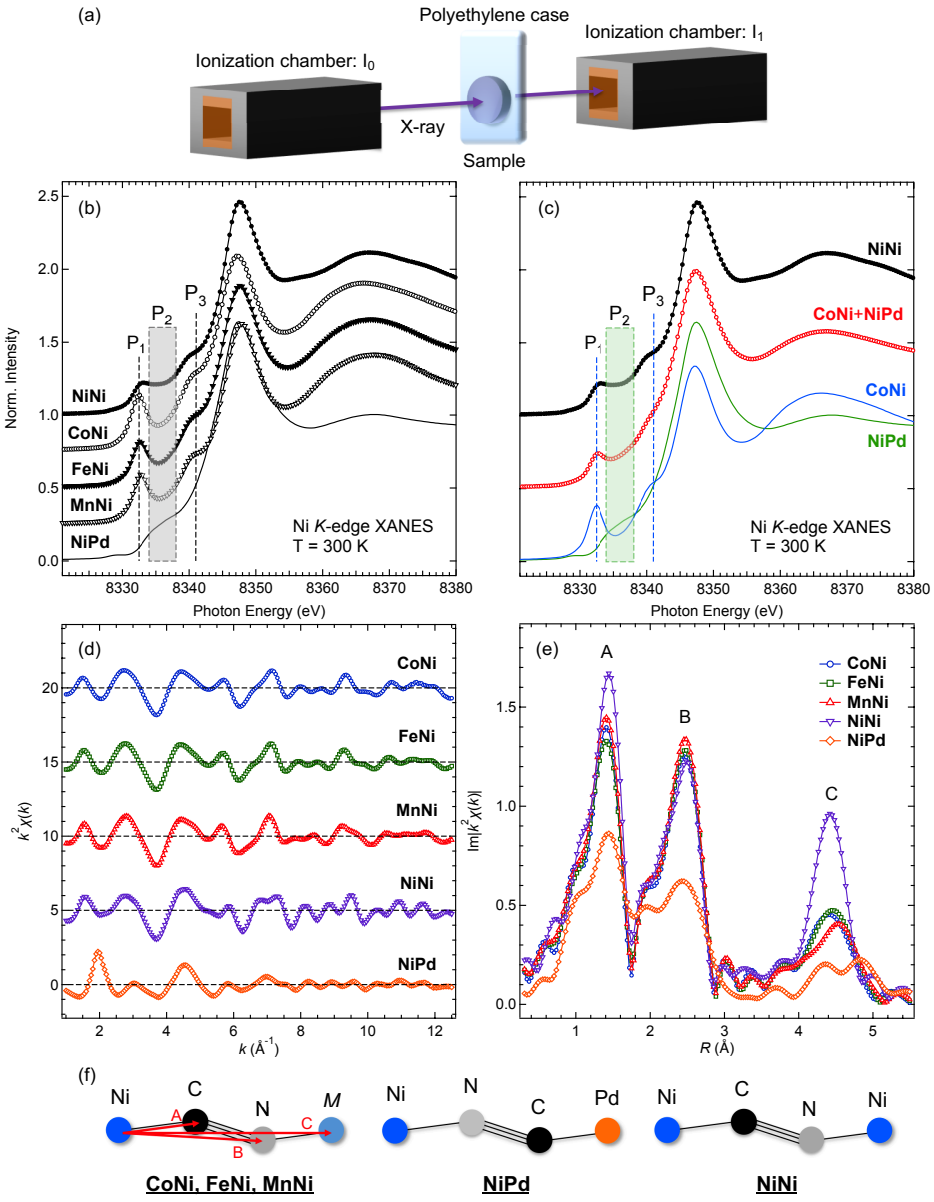

Fig. S6. (Color online) (a) Schematic of the experimental geometry of Ni *K*-edge hard X-ray absorption spectroscopy in transmittance yield mode at 300 K. (b) Comparison with Ni *K*-edge X-ray absorption near-edge spectra of ***M*Ni**, and **NiPd**. (c) Comparison with Ni *K*-edge X-ray absorption near-edge spectra of **NiNi** and the averaged spectra of **CoNi**, and **NiPd**. (d) Ni *K*-edge EXAFS oscillation of ***M*Ni**, and **NiPd**. (e) The radial distance spectra of Ni in ***M*Ni** (*M* = Ni, Co, Fe, Mn) and **NiPd** obtained by the Fourier transform. (f) The illustration of the corresponding radial distance A, B, and C in panel (e).

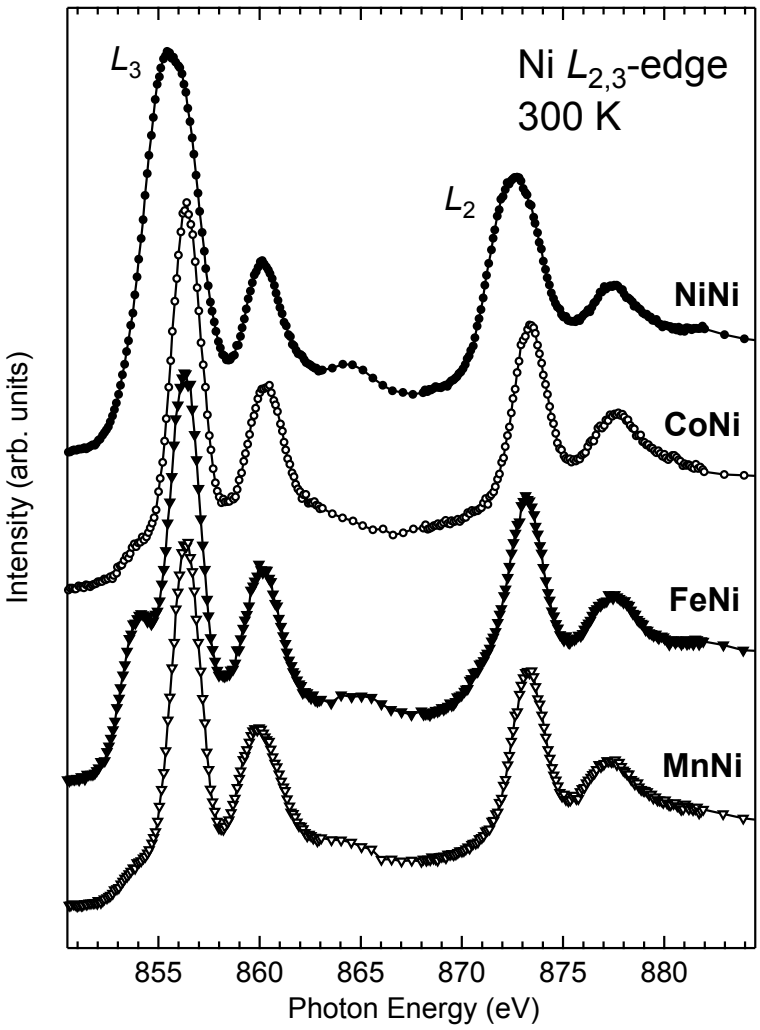

Fig. S7. (Color online) Comparison with Ni $L_{2,3}$-edge XAS spectra in PEY mode of ***M*Ni** (*M* = Mn, Fe, Co, Ni).

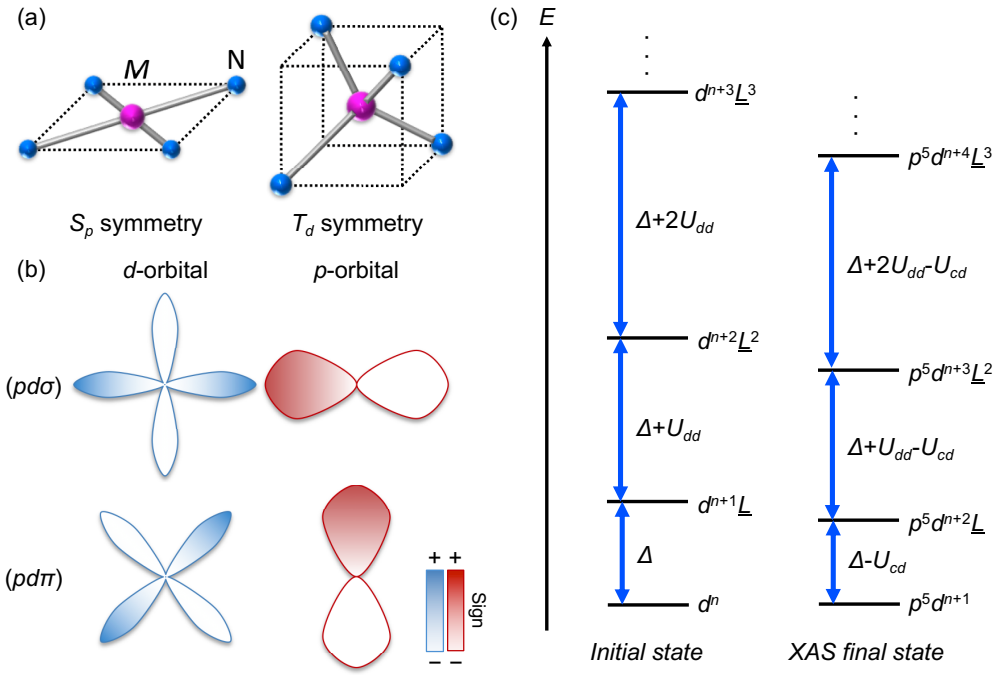

Fig. S8 (a) MN$_4$ single cluster under S_p and T_d symmetry. (b) Schematic of the Slater-Koster parameter ($pd\sigma$) and ($pd\pi$). (c) Schematic energy diagram of each $|d^n\rangle$ and $|d^{n+m}\underline{L}^m\rangle$ configurations for the initial and XAS final states when the hybridization is zero.

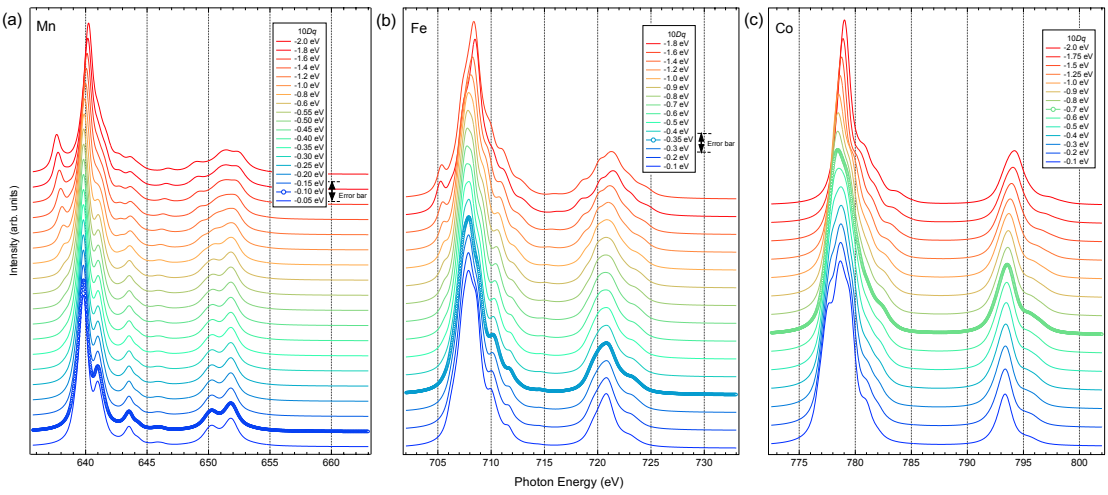

Fig. S9. 10Dq dependence of the calculated $L_{2,3}$-edge XAS spectra for Mn, Fe, and Co.

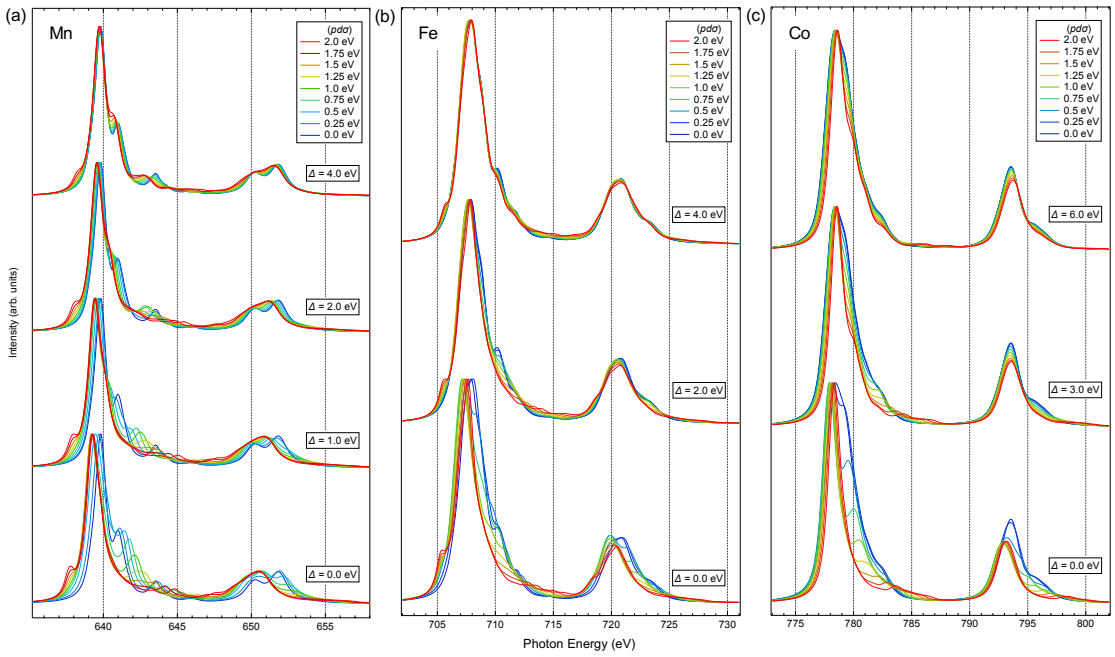

Fig. S10. (*pdσ*) dependence of the calculated $L_{2,3}$-edge XAS spectra. 10*Dq* was set to -0.1 eV for Mn, -0.35 eV for Fe, and -0.7 eV for Co, while U_{dd} was constantly set to 6.5 eV, respectively.

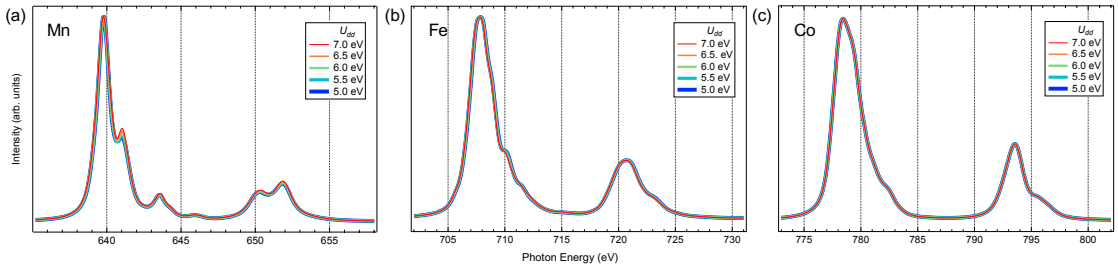

Fig. S11. U_{dd} dependence of the calculated $L_{2,3}$-edge XAS spectra. 10*Dq*, Δ, and (*pdσ*) were set to -0.1 eV, 0.0 eV, 0.15 eV for Mn, -0.35 eV, 4.0 eV, 1.0 eV for Fe, and -0.7 eV, 4.5 eV, 0.125 eV for Co, respectively.

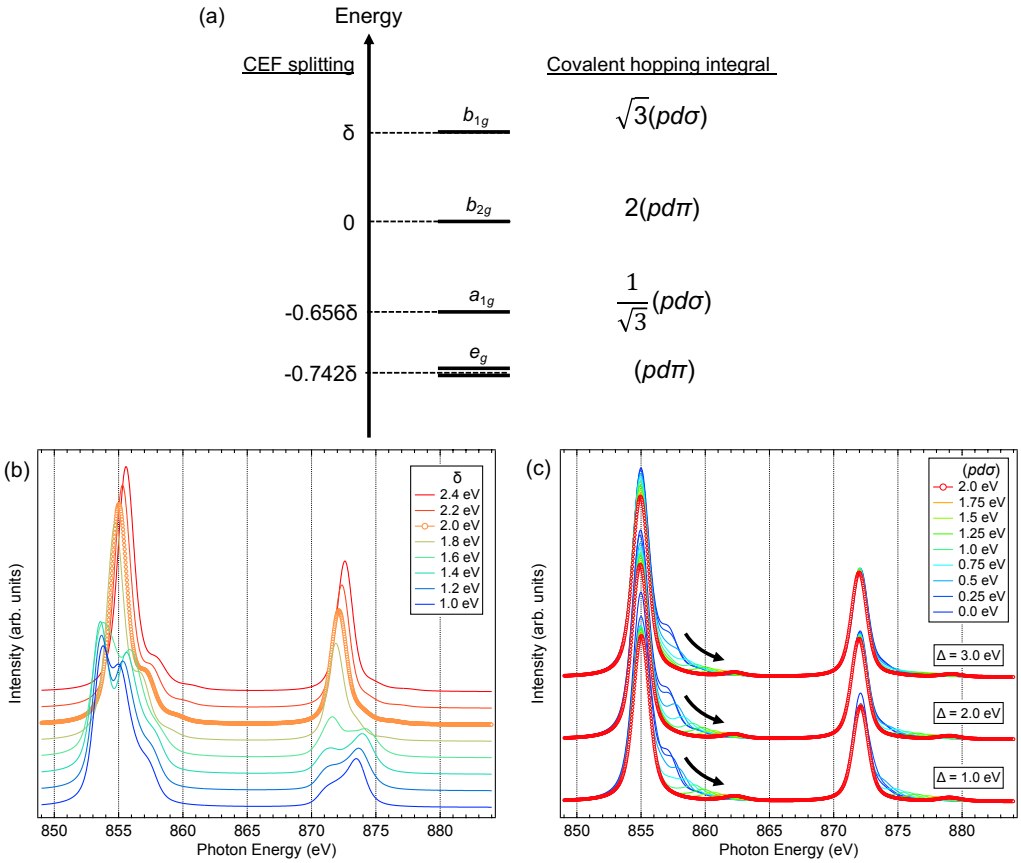

Fig. S12. (a) Schematic energy diagram of CEF splitting for *d* orbital under S_p symmetry. Covalency-hopping integrals formation for each orbital is also shown. (b) δ dependence of the calculated $L_{2,3}$-edge XAS spectra for Ni. (c) ($pd\sigma$) dependence of the calculated $L_{2,3}$-edge XAS spectra. δ was set to 2.0 eV, while U_{dd} was constantly set to 6.5 eV, respectively.

References

1. J. Rodríguez-Hernández, A. A. Lemus-Santana, C. N. Vargas, E. Reguera, Comptes Rendus Chim. **2012**, 15, 350–355.2
2. R. Ohtani, H. Matsunari, T. Yamamoto, K. Kimoto, M. Isobe, K. Fujii, M. Yashima, S. Fujii, A. Kuwabara, Y. Hijikata, S. Noro, M. Ohba, H. Kageyama, S. Hayami, Angew. Chem. Int. Ed. **2020**, 59, 19254-19259.
3. H. Yoshino, K. Yamagami, H. Wadati, H. Yamagishi, H. Setoyama, S. Shimoda, A. Mishima, B. Le Ouay, R. Ohtani, M. Ohba, Inorg. Chem., **2021**, 60, 3338-3344.
4. V. Favre-Nicolin and R. Černý, J. Appl. Crystallogr., **2002**, 35, 734–743.
5. F. Izumi and K. Momma, Solid State Phenom., **2007**, 130, 15–20.
6. B. Ravel, M. Newville, J. Synchrotron Rad. 2005, **12**, 537-541.
7. A. Tanaka, T. Jo, J. Phys. Soc. Jpn., 1994. **63**, 2788-2807.
8. R. D. Cowan, The Theory of Atomic Structure and Spectra (University of California Press, Berkeley, CA), 1981.
9. I. B. Bersuker, Electronic Structure and Properties of Transition Metal Compounds 2nd ed. (Wiley, New York), 1996.
10. J. C. Slater and G. F. Koster, Phys. Rev. 1954. **94**, 1498-1524.
11. J. Zaanen, C. Westra, and G. A. Sawatzky, Phys. Rev. B, 1986, **33**, 8060-8073.
12. A. E. Bocquet, T. Mizokawa, T. Saitoh, H. Namatame, and A. Fujimori, Phys. Rev. B, 1992, **46**, 3771-3784.
13. A. E. Bocquet, T. Mizokawa, A. Fujimori, M. Matoba, and S. Anzai, Phys. Rev. B, 1995, **52**, 13838-13849.
14. G. van der Laan, J. Zaanen, G. A. Sawatzky, R. Karnatak, and J.-M. Esteva Phys. Rev. B, 1986, **33**, 4253-4263.